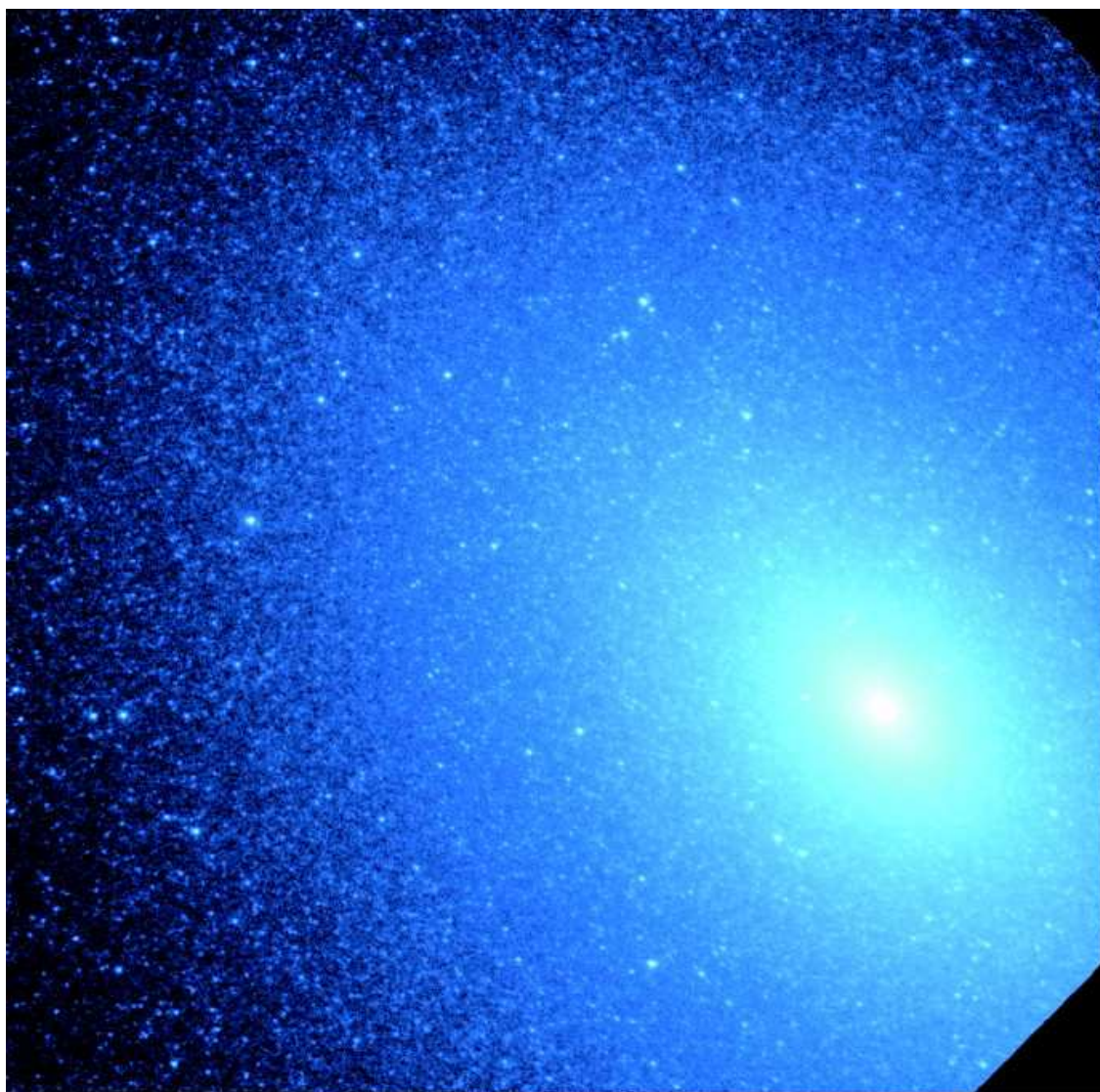


An analysis of the UV properties and single stellar  
population parameters of a sample of early-type galaxies  
from *SDSS* and *GALEX*

Arjen Siegers  
Supervisor: Scott Trager

April 3, 2006



**Cover illustration:** False-colour image of M32 by Brown et al. (2000).

## ABSTRACT

Recent results from *GALEX* (Yi et al. 2005) suggest that  $\sim 15\%$  of early type galaxies show evidence of recent ( $\sim 100$  Myr) star formation. This is inferred from enhanced UV fluxes and blue (FUV-NUV) colours. We obtain spectra and UV colours for 322 galaxies from the Sloan Digital Sky Survey and the *GALEX* database. Single stellar population (SSP) ages were obtained from the absorption features in the optical spectra using the method employed by Trager (2000a & 2000b). This report discusses our efforts to find an anti-correlation between the (FUV-NUV) colours and the optical SSP ages of the galaxies, i.e. a bluer (FUV-NUV) colour should trace recent star formation, given the predictions of stellar population models. We do not see such an anti-correlation; we suggest that the UV colours and the optical absorption line strengths arise from different stellar populations.

---

# Contents

<b>1</b>	<b>Introduction</b>	<b>4</b>
<b>2</b>	<b>Data</b>	<b>7</b>
2.1	UV-colours and stellar population parameters from the literature . . . . .	7
2.2	<i>SDSS</i> . . . . .	8
2.3	<i>GALEX</i> . . . . .	10
2.4	Merging the samples . . . . .	11
<b>3</b>	<b>Method</b>	<b>12</b>
3.1	Processing the <i>SDSS</i> spectra . . . . .	12
3.2	<i>GALEX</i> photometric reduction . . . . .	13
3.3	<i>GALEX</i> Extinction correction . . . . .	14
3.3.1	K-corrections . . . . .	15
<b>4</b>	<b>Results</b>	<b>16</b>
4.1	The literature sample . . . . .	16
4.2	Stellar populations from the <i>SDSS</i> spectrometry . . . . .	17
4.3	UV colours from <i>GALEX</i> . . . . .	18
4.4	The combined sample: UV colours vs. $H\beta$ and SSP age . . . . .	19
4.5	The combined sample: Principal Component Analysis . . . . .	19
<b>5</b>	<b>Discussion</b>	<b>22</b>
<b>6</b>	<b>Conclusion</b>	<b>24</b>
<b>A</b>	<b>Data access in <i>SDSS</i> and <i>GALEX</i></b>	<b>27</b>
<b>B</b>	<b>Principal Component Analysis</b>	<b>29</b>
<b>C</b>	<b>Code</b>	<b>32</b>

# 1 Introduction

The spectra of almost all normal<sup>1</sup> early-type galaxies and spiral bulges show a rise in flux at  $\sim 1000 - 2500\text{\AA}$ . This phenomenon is commonly referred to as the ultraviolet upturn.

The first observations of early type galaxies in the ultraviolet (UV) were conducted using the *Observational Astronomical Observatory* (Code 1969). Based on UV photometry of seven early type galaxies, Code and Welch (1979) concluded that early-type galaxies exhibited a large scatter in their ultraviolet energy distributions (Fig. 1, left panel). Subsequent analysis of IUE photometry by, amongst others, Bertola et al. (1980), Bertola et al. (1982) and Oke, Bertola and Cappacioli (1981)(Fig. 1, right panel), shows the ultraviolet upturn phenomenon (or Ultra-Violet eXcess, UVX) in early-type galaxies. The IUE observations also confirmed that the UV light

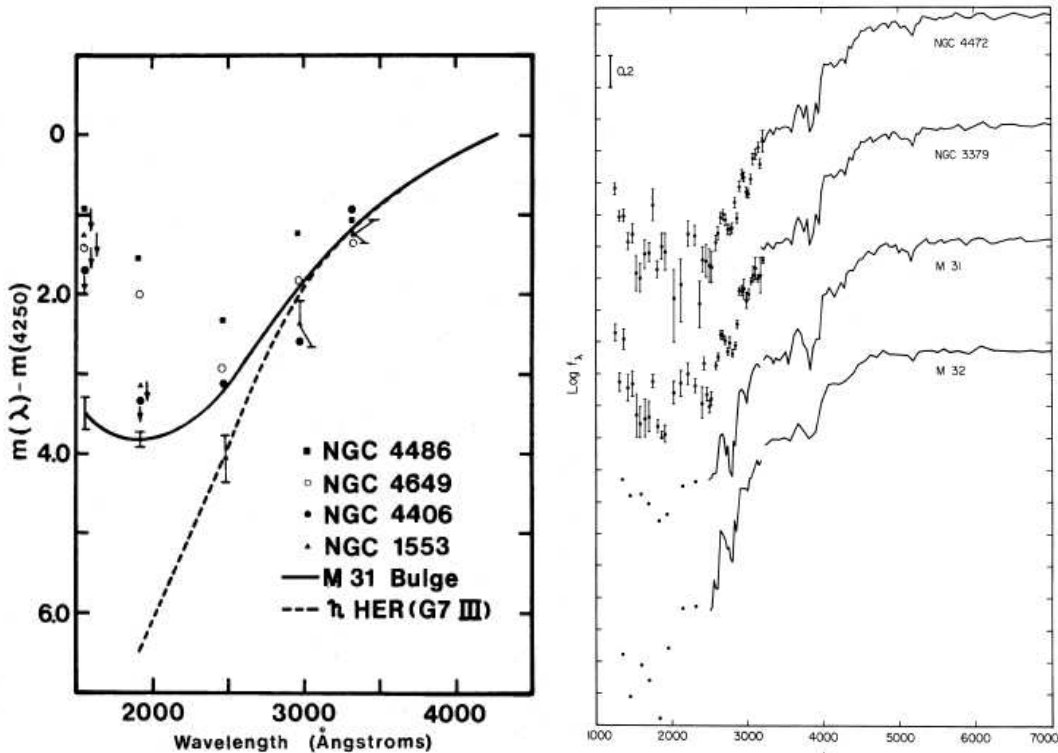


Figure 1: Left: Observations of four early type galaxies, the bulge of M31 and the G7 giant  $\eta$  Her from OAO-2 by Code and Welch (1979) Right: Spectral energy distributions for the elliptical galaxies NGC 3379 and NGC 4472, the bulge of M31 and the dwarf elliptical M32. Below 3200 Å the data are from the IUE, above 3200 Å the data are from the Palomar Hale spectrometer with adjustment for the IUE aperture where necessary (Oke, Bertola and Cappacioli 1981).

distribution over the radius of the galaxy follows the optical luminosity profile, so the sources of the UV should be similar to those of the visual light. In other words, the UV emission is not caused by AGN activity (Oke et al. 1981), but is caused by some stellar component. There are two possible stellar populations that may contribute to the UVX. Since we require a source with an effective temperature of  $\sim 10,000\text{K}$ , we find that both a young stellar population containing massive young stars or one containing stars on the extended horizontal branch and their progeny have the required temperature.

Young stellar populations as a source of the UV upturn were suggested by Tinsley (1972), who proposed a model in which star formation continues in the galaxy, powered by gas falling into

<sup>1</sup>We define normal in the same way as Dorman et al. (1995), i.e. neither active galactic nuclei (AGNs) nor galaxies which show obvious signs of recent star formation.

the central core of the galaxy. This gas can be primordial, i.e. present since the formation of the galaxy, can come from mass loss by red giants, or it can be accreted material. Neutral HI gas has been found in four early-type galaxies (NGC 802, NGC 2328, ESO 118-G34, ESO 027-G21) by Sadler et al. (2005). These galaxies exhibit signs of star formation in their central 1-2 kpc, and in ESO 118-G34 and NGC 2328 HII regions have been observed directly. In order to simulate the effect of a young stellar population on the UV properties of a stellar population, Gunn, Stryker and Tinsley (1981) superimpose the spectra of four different stellar populations derived from their own synthetic population analysis, on the UV spectra of three galaxies (NGC 4472, M31 and M87). They find that a young population is necessary in these systems. Deharveng et al. (2002) propose that low-level residual star formation is responsible for the UV colours of some of the objects in their dataset, much like Yi et al. (2005, see below).

On the other hand, several authors argue that the UVX is caused by an old stellar population (Hills 1971, Welch 1982, Faber 1983). The smoothness of the distribution of the UV light in early type galaxies appears to be an argument against young stars being the source of the UVX, since star formation is usually associated with clumpy OB associations (O’Connell 1999). Hills (1971) showed that the rise in the UV spectrum of M31 was closely matched by the Rayleigh-Jeans tail of a thermal source with  $T_{\text{eff}} \sim 2 \times 10^5 \text{K}$ . He argues that this spectrum could be caused by old, hot horizontal branch (hereafter: HB) stars and the evolutionary phases which follow the HB.

HB stars burn helium in their cores with a hydrogen burning envelope surrounding it. Upon exhaustion of the helium in the core, with helium burning continuing in a shell surrounding the core, the star evolves away from the horizontal branch towards higher luminosities. There are three different cases for the post-HB evolution: AGB, E-AGB and AGB-Manqué (Fig.2). Stars on the red end of the HB, which have high envelope masses ( $M_{\text{ENV}}$ ) and thus lower  $T_{\text{eff}}$ , will evolve up the AGB. On the asymptotic giant branch, the star consists of a carbon core (formed in the triple-alpha process<sup>2</sup> in which helium is burned) surrounded by a helium-burning shell, which in turn is surrounded by a hydrogen burning shell (see e.g. Kippenhahn & Weigert 1994). When the hydrogen shell has burned outwards long enough the temperature of this shell drops and hydrogen burning extinguishes. When the helium burning shell reaches the hydrogen-rich part of the star it will ignite the hydrogen once again. This “thermal pulsing” is however a very unstable phenomenon, and it can move the star over a large distance in the HR diagram (see Fig 32.11 in Kippenhahn & Weigert 1994). The stars evolve to high luminosities and temperatures, possibly form planetary nebulae, and descend the white dwarf cooling curve. Stars with somewhat lower  $M_{\text{ENV}}$  also evolve up the AGB, but leave before the thermal pulsing phase sets in. These stars are known as early-AGB. They continue to high temperatures and luminosities and descend the white dwarf cooling curve. The HB stars with the lowest  $M_{\text{ENV}}$  evolve immediately towards higher luminosities and temperatures, without ascending the AGB, before following the white dwarf cooling curve (Greggio and Renzini 1990, Brown et al. 2000). Since they do not reach the AGB phase, these stars are known as AGB-manqué. An increase in the metallicity of these evolved populations would result in a lower envelope mass. This is due to the higher radiation pressure that is exerted on the envelope because of the larger crosssection of the metals. Thus, the envelope mass, and thus the effective temperature, of these evolved populations is highly dependent on their metallicity.

Yi et al. (1999) describe the evolution of the UV-to-V flux ratio of a stellar population for several chemical evolution models, as illustrated in Fig. 3. In their description, the UV flux starts off high, due to the young hot main sequence stars. When these cool down the UV flux decreases. As the first main sequence stars evolve onto the horizontal branch, the “onset of the UV upturn” begins. During the first few gigayears after the onset of the UV-upturn the relatively short-lived PAGB stars (which evolve from the more massive stars) dominate the UV flux, until the hot (low-mass) HB stars gradually take over. The metallicity of the population will greatly influence the speed of this evolution since mass loss increases with metallicity. So a star with a metallicity substantially higher than solar will evolve faster, as can be seen in Fig. 3: the lines marked C and D which represent models of higher metallicity due to an “infall” model being used to model the chemical

<sup>2</sup>The triple-alpha process consists of the following reactions:  ${}^4\text{He} + {}^4\text{He} \rightleftharpoons {}^8\text{Be}$ ,  ${}^8\text{Be} + {}^4\text{He} \rightleftharpoons {}^{12}\text{C} + \gamma$

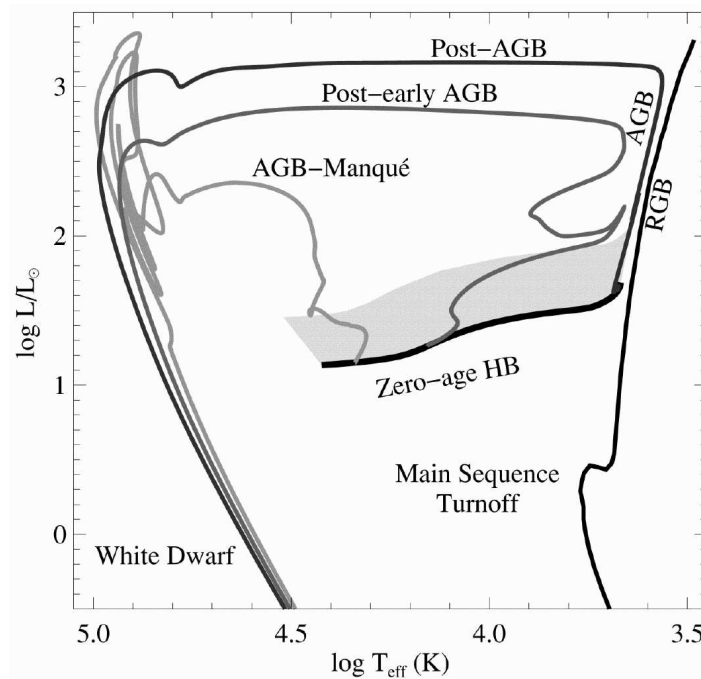


Figure 2: The horizontal branch and the post-HB evolution. Three different scenarios are illustrated arising from different effective temperature and envelope mass. (Brown et al. 2000)

evolution .

Yi et al. (2005) have constructed a near-UV colour-magnitude relation (CMR) for galaxies classified as early-type from the Sloan Digital Sky Survey with data from *SDSS* and *GALEX*. Galaxies were selected using the Bernardi (2003) criteria, which limit the sample to early-type galaxies based on the luminosity profile, concentration factor and absence of emission lines (for a description of these selection parameters see Section 2). Yi et al. define three groups of galaxies based on their FUV-NUV colours. First there are the 'UV weak' systems. These have a low UV flux,  $m(\text{NUV}) - m(r') > 2.74$  ( $F(\text{NUV})/F(r) < 0.008$ ) and  $m(\text{FUV}) - m(r') > 5.24$  ( $F(\text{FUV})/F(r) < 0.008$ ). The UV radiation in these systems is probably due to old stars. The second group is the 'UV-intermediate group'. The FUV flux in these systems is stronger than their NUV flux, that is,  $m(\text{NUV}) - m(r') < 5.24$ , but  $4.49 < m(\text{FUV}) - m(r') < 5.24$  ( $0.008 < F(\text{FUV})/F(r) < 0.016$ ). Old populations such as the HB stars and their progeny discussed before may be capable of producing such a FUV flux, but it is difficult to determine whether the flux is caused by young stars or old ones. Finally, there is the 'UV-strong' group. These systems have either a strong NUV flux ( $m(\text{NUV}) - m(r) < 5.24$ ) or a strong FUV flux ( $m(\text{FUV}) - m(r) < 4.49$ ). Yi et al. find that this 'UV-strong' behaviour can be explained by a recent starburst involving  $\sim 1.2\%$  of the mass of the galaxy with an age of 0.2 Gyr. They find that about 15 % of their sample exhibit signs of recent star formation.

The structure of this report is as follows. Section 2 will review the dataset we constructed from values found in the literature, followed by the datasets from the Sloan Digital Sky Survey database and the *GALEX* database and the selection criteria used to obtain these data. Section 3 discusses the methods used in obtaining linestrengths and stellar population parameters from the *SDSS* spectra. Also, this section contains the corrections made to the *GALEX* photometry. Section 4 contains the results obtained from the datasets. Section 5 discusses these results and puts them into the broader perspective of the general picture of galactic evolution. Section 6 lists our conclusions. Appendices discussing data access in *SDSS* and *GALEX*, principal component analysis and some Python code used in the correction for galactic reddening are included at the end of this report.

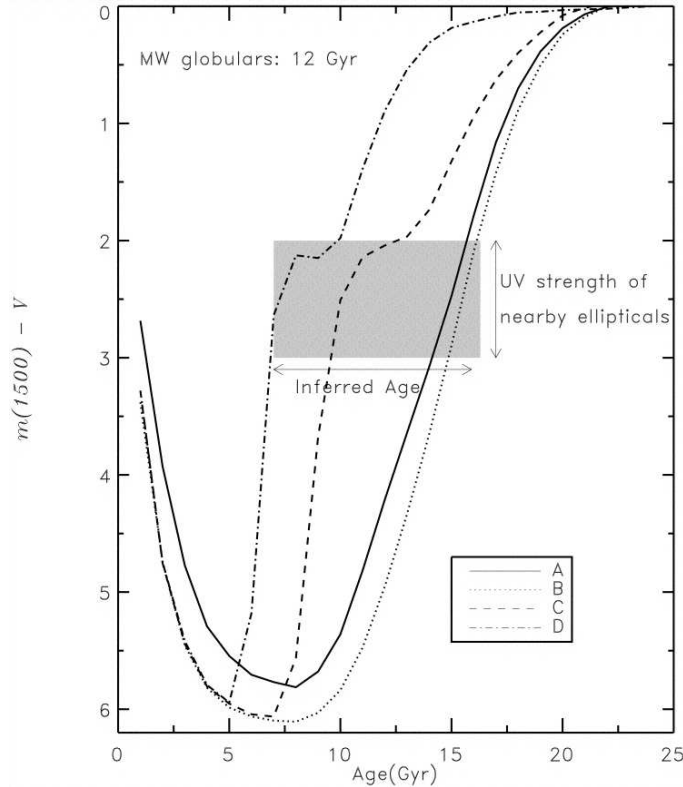


Figure 3: Far-UV colours as a function of stellar population age. Several models are shown. A is an a metal poor population with simple chemical evolution. The other models evolve chemically through infall. The large variation in inferred ages is caused by small changes in the input parameters of the models. Also of note is the asymptotic behaviour of  $m(1500)-V$  at young ages, up to the level of the level produced by the evolved stars. (From Yi et al. 1999)

## 2 Data

This section describes the data that was used over the course of the project. We have used two datasets, the first consisted of 15-25 UV colours<sup>3</sup> taken from Dorman et al. (1995), combined with stellar population parameters derived from line strengths that were published by various authors using the method used by Trager et al. (2005), which will be described in section 3.

### 2.1 UV-colours and stellar population parameters from the literature

Dorman et al. (1995) derive the 15-25 UV colours for 27 galaxies from spectra listed by Burstein et al. (1988) as 'quiescent'. The original UV photometry was performed by the IUE satellite (Kondo 1987).

Single stellar population parameters are obtained by matching a set of optical line strengths to a set of stellar population models, in our case a modified version of the Worthey (1994) models, as described in Trager et al. (2005).

The line strengths were taken from data published by González (1993), Fisher et al. (1996), Trager et al. (1998), Moore et al. (2002) and Mehlert et al. (2003). The data from the González dataset were used in Trager et al. (2000a) to investigate ages and metallicities of early type galaxies. It was selected with the aim of providing a sample of elliptical galaxies which covered

<sup>3</sup>15-25 UV colours are defined as the difference between the flux from a band around  $\sim 1500\text{\AA}$  and a band around  $\sim 2500\text{\AA}$

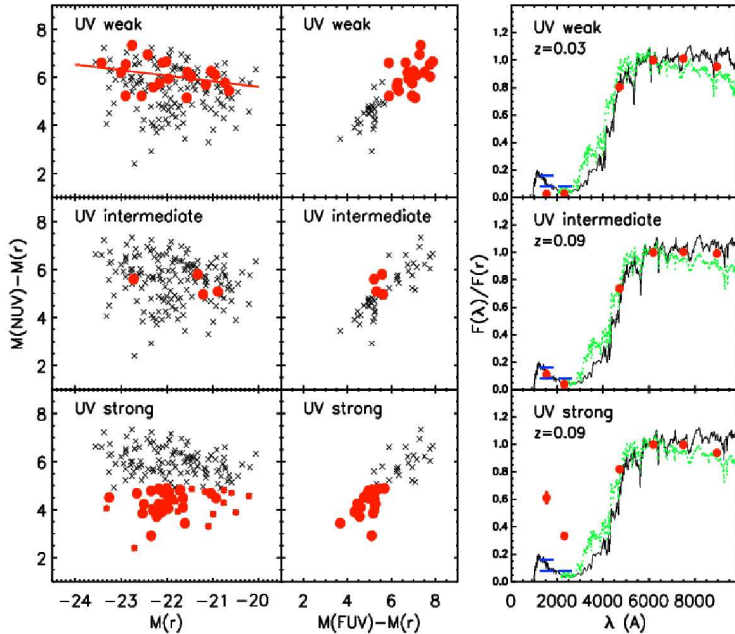


Figure 4: UV-colour magnitude relations and colour-colour relations in early type galaxies, from Yi et al. (2005). Shown here are colours derived from the modelmagnitudes from *GALEX* and the MAG\_AUTO magnitudes from *GALEX*.

the full range of properties colour, line strength and velocity dispersion. Therefore, it is more a *volume-limited* sample. Therefore, it contains more dim, blue, weak-lined, low-dispersion galaxies than would be found in a magnitude-limited sample. This sample also includes NGC 224, the bulge of M31. The galaxies in the sample are referred to as local “field” elliptical galaxies (Trager et al.2000a). From this dataset we used the ellipticals NGC 3379, NGC 4472, NGC 4552 and NGC 4649. It also includes NGC 224 (M32), and NGC 221, the dwarf elliptical companion to M31. The Fisher et al. (1996) sample consists of Lick/IDS indices  $H\beta$ ,  $Mgb$ , and  $Fe$  for 20 S0 systems, and 2 elliptical galaxies. The galaxies used from this dataset are NGC 3115, NGC 4382 and NGC 4762. All three of these are S0 systems. Trager et al. (1998) present the definitive absorption line strengths for the galaxies in the Lick/IDS database. This database was used to create the so-called Lick/IDS absorption line index system, which was intended to extract nearly all the useful absorption features in in the Lick/IDS stellar and galaxy database. The Kuntschner data consists of line strengths on the Lick/IDS system of early-type (both elliptical and lenticular) galaxies from the Fornax cluster. These galaxies have been selected to obtain a complete magnitude-limited sample down to an absolute  $B$ -magnitude of  $B_T = 14.2$ .

The eventual sample consists of 16 early-type quiescent galaxies for which both UV data and stellar population parameters were available, and the bulge of M31. The properties of this sample will be discussed in section 4. The Kuntschner data consists of early-type (both elliptical and lenticular) galaxies from the Fornax cluster. These galaxies have been selected to obtain a complete magnitude-limited sample down to an absolute  $B$ -magnitude of  $B_T = 14.2$ .

## 2.2 SDSS

The Sloan Digital Sky Survey (*SDSS*) is the largest (by depth $\times$ area) optical sky survey undertaken so far. It is intended to cover a quarter of the sky, and will eventually collect spectra of  $\approx 10^6$  galaxies and hundreds of thousands of other objects (stars, quasars, etc.) (Stoughton et al. 2002). The survey uses a 2.5 meter telescope located at Apache Point, New Mexico which

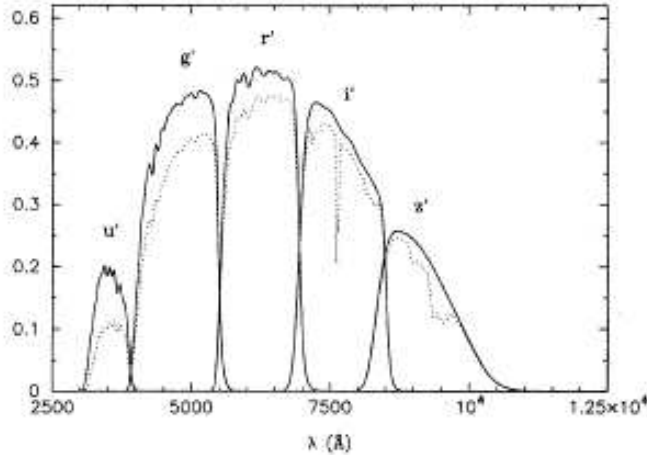


Figure 5: Response functions of the *SDSS* photometric system (Fukugita et al. 1996). The dashed curves represent the response function including atmospheric transmission at 1.2 airmasses at the altitude of the Apache Point observatory.

performs both photometry and spectrometry. Photometry is performed on five bands labelled  $u'$ ,  $g'$ ,  $r'$ ,  $i'$ ,  $z'$ , which cover 3000 - 11000 Å. These bands are defined on the AB system, which is defined as (Fukugita et al. 1996):

$$AB_{\nu} = -2.5 \log f_{\nu} (\text{ergs s}^{-1} \text{cm}^{-2} \text{Hz}^{-1}) - 48.60 \quad (1)$$

Fig 5. shows the response function for the various bands. In our analysis we will only use the red  $r'$  band. The data processing pipeline of the *SDSS* produces several types of magnitudes for observed galaxies: the fiber magnitude, which is a magnitude taken from the flux from a 3'' spectroscopic fiber, the Petrosian magnitude, which measures galaxy fluxes within a circular aperture whose radius is defined by the shape of the azimuthally averaged light profile, and magnitudes matched to a galaxy model. Two different models are used: **1**) a pure de Vaucouleurs profile:

$$I(r) = I_0 \exp -7.67 \left[ (r/r_{\text{eff}})^{(1/4)} \right] \quad (2)$$

(truncated beyond 7  $r_{\text{eff}}$  to go smoothly to zero at 8  $r_{\text{eff}}$ ) and **2**) a pure exponential profile:

$$I(r) = I_0 \exp(-1.68r/r_{\text{eff}}) \quad (3)$$

(truncated beyond 3 $r_{\text{eff}}$  to smoothly go to zero at  $r_{\text{eff}}$ ).

These model fits yield the effective radii for both models, as well as the magnitudes associated with these models. The magnitude corresponding to the model which best fits the isophotes in the  $r$  band is listed as `modelMag`. Finally, the magnitudes corresponding to the flux contained to the 3'' spectroscopic fibers (see below) are listed for each of the five bands. Reddening corrections are derived from the Schlegel et al. (1998) dustmaps, and the corresponding colour excesses are listed for each observation (the dereddening is explained in §3.2). The photometric properties of each object are listed in the `photObjA11` table in the *SDSS* on-line database<sup>4</sup>

The *SDSS* telescope performs spectroscopy using fibers which each subtend 3''. The galaxies in the spectroscopic sample are selected from photometric objects which have previously been observed in the photometric survey and classified as 'extended'. The spectra are processed by two pipelines `spectro2d` and `spectro1d`. the `spectro2d` pipeline reduces the raw data and produces the final spectra, noise estimates and mask arrays which are analysed by the `spectro1d` pipeline,

<sup>4</sup>For further details on the *SDSS* database, see Appendix A.

which determines redshifts, classifies the object by type and measures lines in the spectrum. These properties are listed in the table `specObjA11` in the *SDSS* database.

The requirements we put on the galaxies in our dataset limited the sample to early-type galaxies which do not show obvious signs of star formation or evidence of AGN activity. We adopt the same criteria as used by Yi et al. (2005), who have used the sample selected by Bernardi et al. (2004). Bernardi et al. conducted a survey of the properties of early-type 'quiescent' galaxies from the *SDSS*. Their criteria have been chosen to obtain these galaxies: **a)**  $r_{90}/r_{50} > 2.5$ , this is the ratio between the radii which contain 90 % and 50% of the Petrosian flux respectively. This high concentration index will ensure that that most of the early-type galaxies are selected. **b)** A likelihood of the de Vaucouleurs model fit at least 1.03 times larger than that of the exponential model; **c)** A PCA classification index  $< 0.1$ . This classification index has been developed by Connolly et al. (1995) and expanded by Connolly and Szalay(1999). They use principal component analysis on a sample of 10 galaxy spectral energy distributions, from different morphologies, to generate a set of 10 eigenspectra such that each galaxy spectrum,  $f_\lambda$  can be expressed as a linear combination of orthogonal eigenspectra,  $e_{i\lambda}$ :

$$f_\lambda = \sum_i a_i e_{i\lambda} \quad (4)$$

Here,  $\lambda$  is the wavelength dimension,  $i$  is the number of the eigenspectrum and  $a_i$  are the coefficients of the linear combination. The principal component analysis provides us with a measure of the contribution of each of the eigenspectra. It is found that only the first two eigenspectra are relevant in determining the morphology of the galaxy. This is listed in the *SDSS* database as the `eClass` parameter, which is equal to  $\text{atan}(-a_2/a_1)$ , where  $a_1$  and  $a_2$  are the first two eigenspectra; **d)** We require intact spectra, so we want to eliminate any spectra with masked areas. This is done by selecting galaxies with the flag `zWarning` set to zero; **e)** The redshift inferred from the spectra should be  $z < 0.3$ . This is necessary because the *SDSS* main galaxy sample was selected is apparent magnitude limited in  $r^*$ . At  $z \geq 0.3$  the selection criteria for galaxies in the *SDSS* are different, since they belong to the Luminous Red Galaxy sample. In order to keep the sample as magnitude limited as possible, we choose to restrict our sample to  $z \leq 0.3$ ; **f)** We limit our sample to observations with  $S/N > 10$ , since the magnitudes used by *SDSS* are based on the  $\sinh^{-1}$  system developed by Lupton et al. (1999), which start to diverge from the regular Pogson magnitudes for  $S/N \lesssim 10$ . Using these criteria, we obtain 101701 galaxies from the *SDSS* Third Data Release. As can be seen in figure 6, the resulting sample exhibits a very clear Malmquist bias, i.e. it is not absolute-magnitude limited.

## 2.3 GALEX

The *Galaxy Evolution Explorer (GALEX)* satellite performs the first all-sky imaging and spectroscopic survey in the ultraviolet (1350-2750 Å). Its primary objective is to study star formation in galaxies and its evolution in time. The technical description of the *GALEX* mission is given by Martin et al. (2005). It observes galaxies in the far-ultraviolet (FUV, 1350-1750 Å), at a resolution of  $4''.5$ , and in the near-ultraviolet (NUV, 1750-2750 Å) with a resolution of  $6''.0$ . Several surveys are being conducted as part of the *GALEX* project. Two of these are of special interest for this project:

*All-sky imaging survey(AIS)*- The goal of the AIS is to obtain a complete survey of the sky down to a sensitivity of  $m_{AB} \simeq 20.5$ , which is comparable to the Sloan Digital Sky Survey (*SDSS*) spectroscopic ( $m_{AB} = 17.6$ ) limit. *Medium Imaging Survey (MIS)*- The MIS covers 1000 deg<sup>2</sup> with extensive overlap with the *SDSS*. MIS exposures usually take a single eclipse, lasting about 1500s, with a sensitivity of  $m_{AB} \simeq 23$ , net several thousand objects at once and are well matched to the photometric limits used in the *SDSS* survey (These are the limits imposed on the survey itself, not the selection criteria mentioned in the previous section).

The *GALEX* homepage at the Multimission Archive (<http://galex.stsci.edu/GR1/>) has an SQL interface much like that used on the *SDSS*. For more information, see Appendix A: Data access in *SDSS* and *GALEX*. The same selection criteria as listed by Bernardi et al. (2003) were

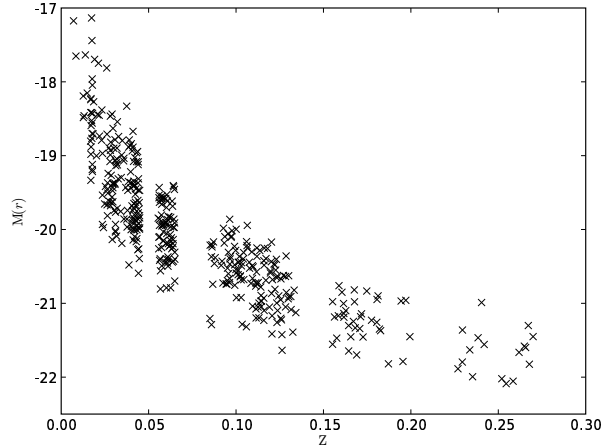


Figure 6:  $r$ -band magnitudes versus redshift for the galaxies in our dataset. As can be seen, the limiting magnitude increases with redshift, signifying a Malmquist bias in the sample. The clear bands in the distribution are caused by the selection of galaxies without fill-in by telluric lines. (For this selection and other operations performed on the optical magnitudes, see section 3.1)

used, with one difference, the signal to noise ratio is not listed in the *GALEX* database. Without this requirement, we found 17103 galaxies in the *GALEX* database. This problem was fixed by matching the two datasets. Our *GALEX* sample consists of aperture magnitudes which were reduced by the pipeline using SExtractor<sup>5</sup>. We chose to use the FUV\_APER\_3 and NUV\_APER\_3, these are the third fixed aperture magnitude listed in the *GALEX* database, and they correspond to the apparent magnitude from the flux through a 5'' aperture.

## 2.4 Merging the samples

After obtaining the samples as discussed in the previous section, we looked for matches in the two samples. Due to the extra limit imposed on the *SDSS* sample, this was reduced to 6680 objects. However, the difference in spatial resolutions between *GALEX* (4.5'' in FUV, 6'' in NUV) and *SDSS* (3'' fibers for each spectrum) caused objects in *GALEX* to be matched to two or more *SDSS* sources. In these cases we have found it prudent to remove the object altogether. Our final sample consisted of 322 galaxies.

<sup>5</sup>A very good SExtractor manual can be found at: <http://www-int.stsci.edu/~holwerda/se.html>

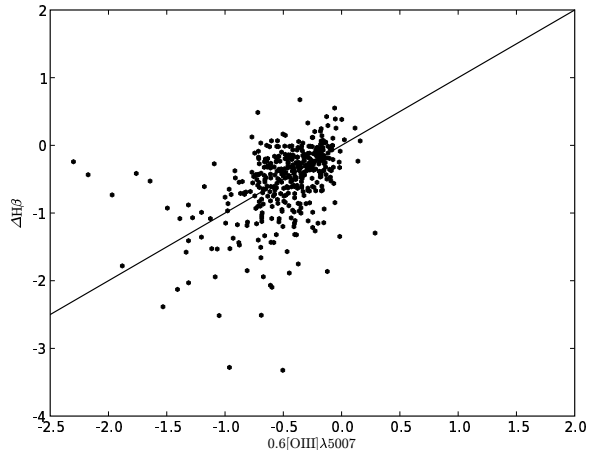


Figure 7: Comparison of the two corrections for  $H\beta$  emission. The  $H\beta$  emission calculated by the MPA group is plotted on the vertical axis, while the correction derived from the [OIII] line strength is plotted on the horizontal axis.

### 3 Method

#### 3.1 Processing the *SDSS* spectra

From the spectra which we took from the *SDSS* we derived Lick/IDS line strengths by using the program *SPINDEX2* (Trager et al. 2005). It reads the redshift and the velocity dispersion of the galaxy from the FITS header accompanying the spectrum. The redshifts are required to put the spectrum in a 'rest-frame', so that the line indexes can be placed on the spectrum. The  $H\beta$  absorption line strength can be subject to  $H\beta$  emission. To correct for this emission we have used the relation between  $H\beta$  emission and [OIII] $\lambda$ 5007 emission line strength given by Trager et al. (2000a):

$$\Delta H\beta = 0.6EW([OIII]\lambda 5007) \quad (5)$$

(Equation 2 in Trager et al. 2000a lists a value of 0.7 for this conversion, but 0.6 is deemed more suitable for a sample containing only normal, non-AGN early-type galaxies.) The [OIII] emission data was taken from the emission line catalogue of the Max Planck Institute for astrophysics (MPA) in Garching<sup>6</sup>. This dataset also provides  $H\beta$  emission line strengths which could be used to correct the absorption directly, but we have found very little difference between these two methods, as can be seen in figure 7. The observed spectrum of a galaxy is a convolution of the integrated spectrum of its stellar population and the distribution of the line-of-sight velocity distributions of its stars. The velocity dispersions broaden the spectral features, making them appear weaker (Trager et al. 1998). To correct for this broadening we use the program *SCORRECT*. This program corrects each index on the Lick/IDS system using the velocity-dispersion corrections as published in Trager et al. (1998). These corrections have been calculated by convolving the original Lick/IDS stellar spectra were convolved with broadening functions of various velocity dispersions, up to 450 km s<sup>-1</sup>. The index strengths on these convolved indices were measured, and a third order polynomial was fitted to the ratios between the convolved and the unconvolved indices for the indices versus velocity dispersion. The correction is then:

$$I_{j,k}^{\text{corr}} = C_j(\sigma_v) \times \langle I_j \rangle_k \quad (6)$$

<sup>6</sup>This catalogue can be found at: [http://www.mpa-garching.mpg.de/SDSS/DR2/Data/emission\\_lines.html](http://www.mpa-garching.mpg.de/SDSS/DR2/Data/emission_lines.html)

Here  $\langle I_j \rangle_k$  is the mean value of index  $j$  of galaxy  $k$ , and  $C_j(\sigma_v)$  is the velocity-dispersion correction:

$$C_j(\sigma_v) = \sum_{i=0}^3 c_{ij} \sigma_v^i \quad (7)$$

Where  $c_{ij}$  are the coefficients from the aforementioned polynomial for index  $j$ , and  $\sigma_v$  is the velocity dispersion. These operations were performed using the program `SCORRECT`. Another problem in obtaining the Lick/IDS line strengths is the possibility that they are redshifted onto telluric lines. We removed galaxies from the dataset which had redshifts that caused the Lick/IDS indices for H $\beta$ , Mgb, Fe5270 and Fe5335 to be within 7.5 Å of the central wavelength of these strong telluric lines.

The distribution of the errors in the resulting H $\beta$  line strengths is shown in Figure X. As can be seen, most of the errors were  $\leq 0.3\text{Å}$ , and galaxies with a larger error in the H $\beta$  line strength were removed from the sample.

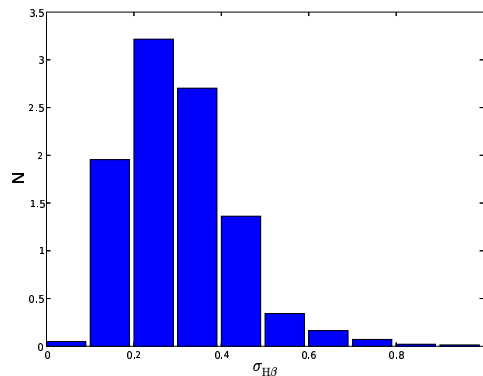


Figure 8: Distribution of the errors in the H $\beta$  linestrengths.

Finally, those galaxies were removed for which velocity dispersion data was not available. In order to obtain the stellar population parameters we use a modification of the Worthey (1994) stellar models, with additional response functions to provide the enhancement factor  $[E/Fe]^7$ . The H $\beta$ , Mgb, Fe5335 and Fe5270 line strengths of the galaxies are fitted by a non-linear least squares fit to the line strengths of models of various ages, metallicities and enhancement ratios.

As a diagnostic, we project our sample on age metallicity grids as generated by these models in H $\beta$ -[MgFe] space and in Mg- $\langle Fe \rangle$  space. Here,  $\langle Fe \rangle$  and [MgFe] are defined as:

$$\langle Fe \rangle \equiv \frac{1}{2}(\text{Fe5270} + \text{Fe5335}) \quad (8)$$

$$[\text{MgFe}] = \sqrt{\text{Mg}\langle Fe \rangle} \quad (9)$$

Eventually, the sample consisted of 496 galaxies for which stellar population parameters were determined. This sample is shown in Fig.11, projected on a Worthey (1994) age-metallicity grid. A number of galaxies fall outside the age-metallicity grid (i.e. they have age  $\leq 18$  Gyr and  $[Z/H] \leq 0.5$ ) and have been rejected in the further analysis, reducing the dataset to 322 galaxies.

### 3.2 GALEX photometric reduction

The FUV and NUV magnitudes from *GALEX* are *apparent* magnitudes. In order to compare them in a meaningful way, we need to convert these to the absolute magnitude. The absolute

<sup>7</sup>The enhancement factor is defined as the mass fraction of elements which are specifically enhanced in the models. This is defined as  $[Fe/H] = [Z/H] - A[E/Fe]$ , where  $A$  is a normalized variable used to quantify the enhancement.

magnitude of an object is defined as the magnitude the object would have if it were located at a standard distance  $D$ , which is taken to be equal to 10 pc. This means that we need to correct for the dimming caused by the distance of the object, which is explained by the inverse square law:

$$f = \left(\frac{D}{d}\right)^2 F \quad (10)$$

Also, there is the problem of extinction by interstellar dust and gas. Both the *GALEX* and *SDSS* databases provide the colour excess,  $E(B - V)$ , for each of the galaxies. This colour excess is defined as the difference between the intrinsic colour and the apparent colour of the galaxy. Finally, there is also the K-correction, which will be discussed in section §3.2.1.

The absolute magnitude is then:

$$M_\lambda = m_\lambda - \log_{10}(d) + 5 - A_\lambda - K_\lambda, \quad (11)$$

where  $d$  is the luminosity distance<sup>8</sup> in parsecs,  $A_\lambda$  is the extinction by interstellar gas (we ignore internal extinction in the galaxies themselves, since we do not have a way of properly measuring this), and  $K_\lambda$  is the K-correction at wavelength  $\lambda$ .

### 3.3 *GALEX* Extinction correction

The colour excess is defined in terms of the extinction in the  $V$ -band,  $A_V$ , and the slope of the extinction curve,  $R_V$ , as:

$$E(B - V) = \frac{A_V}{R_V} \quad (12)$$

For  $R_V$  we estimate a value  $R_V = 3.3$  from figure 3.18 in Binney and Merrifield (1998). In order to apply this colour excess to the UV-magnitudes, we apply the relationship between the extinction in the ultraviolet as derived by Cardelli, Clayton and Mathis (1989) (hereafter: CCM). CCM define the relation between  $A_\lambda$  and  $A_V$  as follows:

$$\left\langle \frac{A(\lambda)}{A(V)} \right\rangle = a(x) + b(x)/R_v(x = 1/\lambda) \quad (13)$$

Where for UV ( $3.3\mu\text{m}^{-1} \leq x \leq 8\mu\text{m}^{-1} \equiv 3030\text{\AA} \leq \lambda \leq 1250\text{\AA}$ ) magnitudes:

$$a(x) = 1.752 - 0.316x - 0.104/[(x - 4.67)^2 + 0.341] + F_a(x) \quad (14)$$

$$b(x) = -3.090 + 1.825x + 1.206/[(x - 4.62)^2 + 0.263] + F_b(x) \quad (15)$$

The conversion from colour excess to extinction parameter is therefore:

$$A(\lambda) = R_V E(B - V)a(x) + E(B - V)b(x) \quad (16)$$

Where  $F_a$  and  $F_b$  are given by:

$$\begin{aligned} F_a(x) &= -0.04473(x - 5.9)^2 - 0.009779(x - 5.9)^3 & (8 \geq x \geq 5.9) \\ F_b(x) &= 0.2130(x - 5.9)^2 + 0.1207(x - 5.9)^3 & (8 \geq x \geq 5.9) \\ F_a(x) &= F_b(x) = 0 & (x < 5.9) \end{aligned}$$

<sup>8</sup>The luminosity distance is the distance a photon takes to travel from a galaxy to an observer, taking into account the cosmic deceleration:  $D_L = \frac{cz}{H_0} \left(1 + \frac{z(1+q_0)}{(1+2q_0z)^{1/2} + q_0z}\right)$ , where  $c$  is the speed of light,  $H_0$  is the local Hubble constant,  $z$  is the redshift and  $q_0$  is the cosmic deceleration parameter, and is defined as:  $q_0 = \frac{\Omega_m}{2} - \Omega_{\Lambda,0}$  (Ryden, 2003). We assume a  $(\Omega_m, \Lambda, H_0) = (0.3, 0.7, 70)$  cosmology, which results in a  $q_0 = -0.55$

### 3.3.1 K-corrections

When an object is observed at a redshift  $z < 1$ , the observed photons will have been emitted at a lower wavelength. Since the spectral energy distribution of a galaxy is not flat, the observed flux will be different from that emitted in the observed waveband. To correct for this problem we use the K-correction<sup>9</sup>, which has already been defined in equation 11. To perform the K-correction, the shape of the spectral energy distribution of the galaxy needs to be known. Blanton (2005), uses stellar population models (e.g. those by Bruzual and Charlot (2003), hereafter BC03) to produce a template spectrum for a galaxy as it would look in a certain restframe.

On average, galaxy spectra can be described by a few template spectra. Blanton (2005) uses template spectra generated by the BC03 stellar population synthesis models and the MAPPINGS-III emission line models. From these models 485 basis templates are taken, which are referred to as  $M_{\lambda,j}(\lambda)$ . Then, for each wavelength (in our case: *GALEX* NUV and FUV bands and the five *SDSS* optical bands  $u, g, r, i, z$ ) a template integrated flux from a spectrum integrated over the appropriate bandpass  $F_{\lambda,i}(\lambda)$  is built from nonnegative combinations of the original basis set of  $N$  templates:

$$F_{\lambda,i}(\lambda) = \sum_j b_{ij} M_{\lambda,j}(\lambda), \quad (17)$$

in units of  $\text{ergs s}^{-1} \text{\AA}^{-1}$ . The integrated flux from model spectrum  $\hat{F}_{\lambda,k}(\lambda)$  would be the sum of these templates:

$$\hat{F}_{\lambda,k}(\lambda) = \sum_i a_{ki} F_{\lambda,i}(\lambda). \quad (18)$$

In order to compare these models to the integrated fluxes of the observed spectra  $f_{\lambda,k}(\lambda)$  of each galaxy  $k$ , the restframe luminosity per unit wavelength is calculated by:

$$F_{\lambda,k} = f_{\lambda,k}[\lambda(1+z)](1+z)(4\pi d_L^2) \quad (19)$$

Now for the discrete integrated fluxes corresponding to spectra at wavelengths  $\lambda_l$ , the relationship between the predicted spectral energy distribution (SED) and the basis set of template spectra is:

$$\hat{F}_{\lambda,k}(\lambda) = \sum_{ij} a_{ki} b_{ij} M_{jl}, \quad (20)$$

and the fit is obtained by optimizing the parameters  $a_{ki}$  and  $b_{ij}$ .

The K-corrections were derived from the *GALEX* MAG\_AUTO magnitudes and the *SDSS* modelmag magnitudes. These corrections were also applied to the colours derived from the fibermag and fixed-aperture magnitudes. This does cause a small discrepancy in the correction, but we expect it to be small.

---

<sup>9</sup>We define the K-correction solely as the correction for the shift in bandpass, and not for the correction of the distance modulus which some authors tend to include in the K-correction.

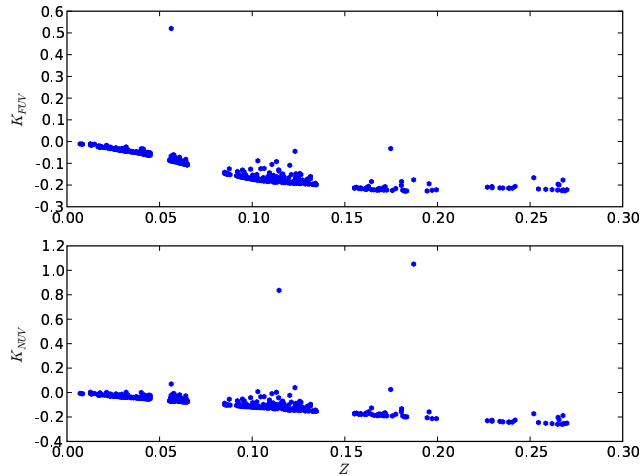


Figure 9: K-corrections in the FUV and NUV bands derived using KCORRECT\_4.3 (Blanton (2005)).

## 4 Results

### 4.1 The literature sample

Table 4 presents the ages and UV colours of the galaxies in the sample drawn from the literature (Section 2.1). The errors are taken from Burstein et al. (1988), since Dorman (et al. 1995), who derived the  $15 - 25$  colours from the Burstein et al. dataset, did not perform their own error analysis, but also used the errors listed by Burstein et al. These errors are on the order of 0.25 mag. for the individual  $15 - V$  and  $25 - V$  colours, so a simple error analysis gives a mean error for the  $15 - 25$  colour,  $\sigma_{15-25} \approx 0.354$  mag, as shown in Fig. 6. The galaxies taken from the Trager et al. (1998) dataset show much larger errors in the SSP ages compared to the rest of this sample. An anti-correlation seems to exist between the  $15-25$  colour and the SSP age of the galaxies.

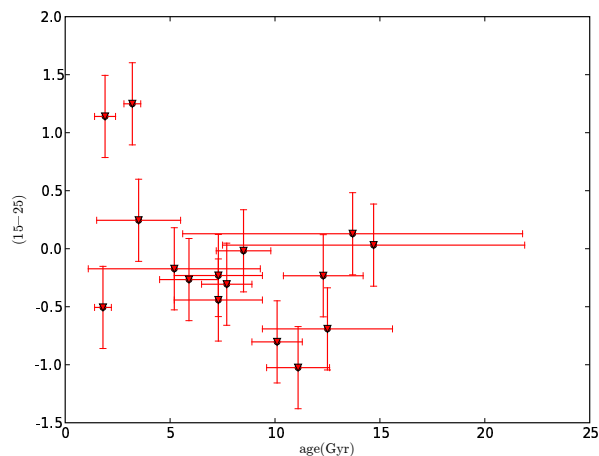


Figure 10: 15-25 UV colors from Dorman et al.(1995) and SSP ages from 16 early-type (E and S0) galaxies.

ID	$\log(\text{age})$	15 – 25	source
NGC221	$3.2 \pm 0.4$	1.249	g93
NGC224	$5.9 \pm 1.4$	-0.266	g93
NGC1399	$12.5 \pm 3.1$	-0.691	k00
NGC1404	$7.3 \pm 2.1$	-0.442	k00
NGC3115	$7.3 \pm 2.1$	-0.231	ffi
NGC3379	$8.5 \pm 1.3$	-0.018	g93
NGC4125	$13.7 \pm 8.1$	0.129	sct98
NGC4374	$12.3 \pm 1.9$	-0.233	g93
NGC4382	$1.9 \pm 0.5$	1.140	ffi
NGC4406	$14.7 \pm 7.2$	0.031	sct98
NGC4472	$7.7 \pm 1.2$	-0.306	g93
NGC4552	$10.1 \pm 1.2$	-0.803	g93
NGC4621	$5.2 \pm 4.1$	-0.173	sct98
NGC4649	$11.1 \pm 1.5$	-1.025	g93
NGC4762	$3.5 \pm 2.0$	0.245	ffi
NGC4889	$1.8 \pm 0.4$	-0.506	m02

Table 1: Galaxies from the literature sample. 15-25 colours were taken from Dorman et al. (1995) and the ages were derived from data listed by Kuntschner (2000) (k00), Fisher et al. (1996) (ffi), Trager et al. (1998) (sct98) and González (1993) (g93) and for one system the ages were calculated using line strength data from Moore et al. (2002) (m02)

## 4.2 Stellar populations from the *SDSS* spectrometry

The final sample from *SDSS* and *GALEX* consists of 385 galaxies. These galaxies are shown in figure 7 as the projection of the  $H\beta$ ,  $[MgFe]$ ,  $Mgb$  and  $\langle Fe \rangle$  linestrengths of these galaxies onto a modified Worthey model grid for an enhancement factor  $[E/Fe]$  similar to the solar value. These galaxies exhibit similar stellar population parameters to those presented by Trager et al. (2000a, 2000b, 2005). The same sample is shown in figure 11 in  $Mg$ - $\langle Fe \rangle$  space showing a preference for  $[E/Fe] = +0.30$ .

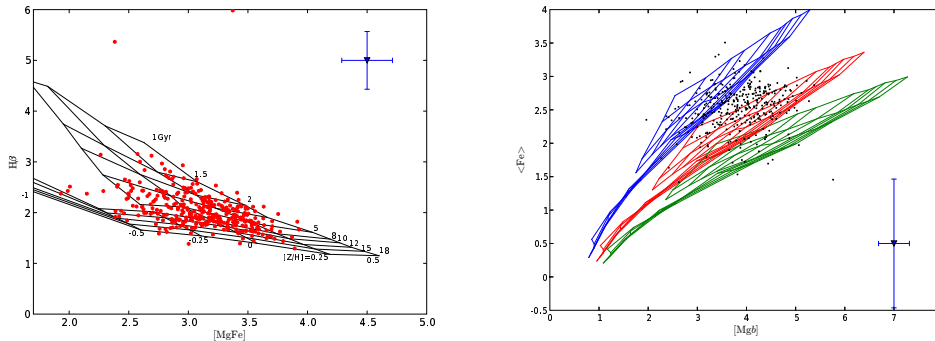


Figure 11: Stellar population parameters of the galaxies in the SDSS sample, show left are the linestrengths in  $H\beta$  and  $[MgFe]$ , projected on an age-metallicity grid produced using the Worthey (1994) stellar population models. The panel on the right shows the sample in  $Mg$ - $\langle Fe \rangle$  space, with three age-metallicity grids corresponding to  $[E/Fe] = 0$ ,  $[E/Fe] = 0.30$  and  $[E/Fe] = 0.50$ .

### 4.3 UV colours from *GALEX*

The galaxies in the sample have been classified using the Yi et al. (2005) scheme into three UV-classes. We have used the *GALEX* MAG\_AUTO FUV and NUV magnitudes and the *SDSS* *r*-band modelmag magnitude, analogous to Yi et al. However, since we perform spectroscopy on light received by a  $3''$  fiber, we show UV-*r* colours and *r*-band magnitudes derived using the *SDSS* fibermagnitudes and the *GALEX*  $5''$  magnitudes. The difference between the plots in Figure 12 and those in Figure 3 can be explained as follows: if we take the radius of the seeing disk to be  $\sim 1''$ , bearing in mind that the *diameter* of the aperture of the spectrograph is  $3''$ , we lose half the light from the system. Therefore, the *r* band fibermagnitudes will differ from the model magnitudes by  $\sim 0.75$  mag.

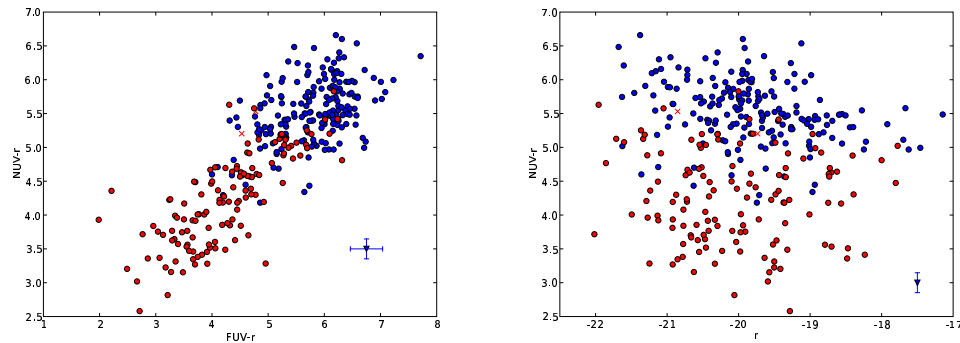


Figure 12: The NUV-*r* vs. *r* colour-magnitude diagram and NUV-*r* vs. FUV-*r* colour-colour diagram for our age and metallicity limited sample. The UV-strong class is represented by red dots, the UV-intermediate by red crosses and the UV-weak by blue dots. The colours in this figure were derived using the  $3''$  fibermagnitudes from *GALEX* and the  $5''$  aperture magnitudes from *GALEX*.

#### 4.4 The combined sample: UV colours vs. $H\beta$ and SSP age

In figure 13 we evaluate the possibility of a relation between the FUV-NUV colour and either the  $H\beta$  line strength or the SSP age. It appears there is no correlation between FUV-NUV and either variable. The errors in the  $H\beta$  absorption line strengths are as much as a factor 10 higher than those used to determine SSP ages by Trager et al. (2000a), which results in the large spread in ages in the left panel of figure 13.

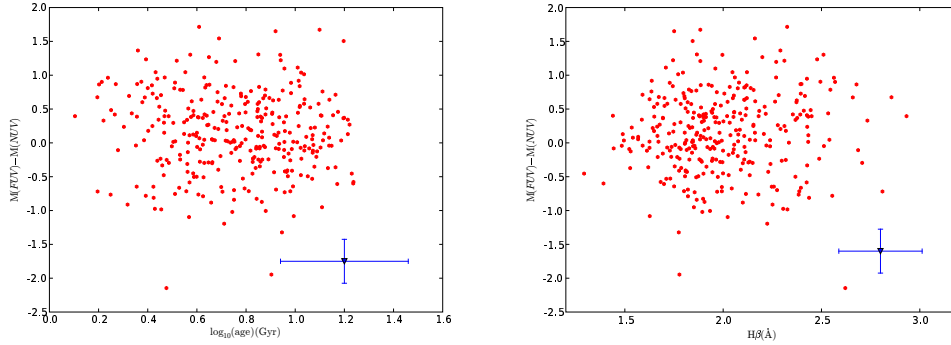


Figure 13: FUV-NUV colours vs  $\log(\text{age})$  (left), and  $H\beta$  (right).

#### 4.5 The combined sample: Principal Component Analysis

The SSP variables age,  $[Z/H]$ ,  $[E/Fe]$ , the line of sight velocity dispersion  $\sigma$  and the FUV-NUV colour span a five-dimensional space. Principal component analysis on the correlation matrix (Murtagh and Heck 1987) was used to investigate the correlations between the parameters in this space. The PCA was performed on the total sample, the galaxies classified as UV-weak and those classified as UV-strong. Since there are only two galaxies in the UV-intermediate it was left out of the analysis.

**The total sample** In Fig 14 we show the projection of the total sample on the first three principal components. In this case the first three principal components contain 80.82 % of the total variance in the dataset.

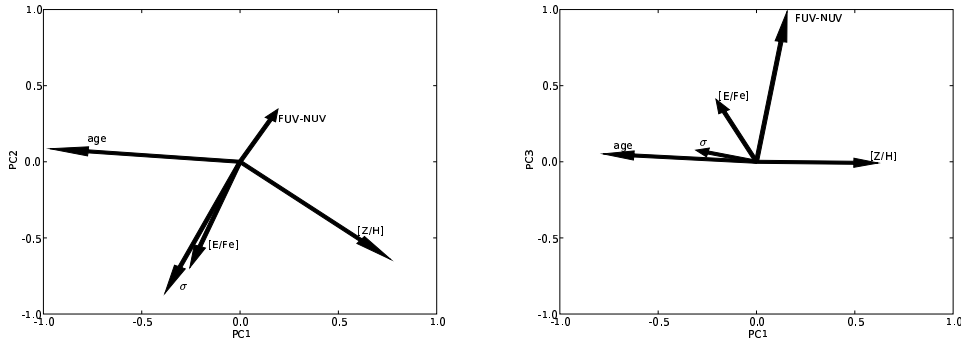


Figure 14: Principal components from the total dataset.

Variable	PC1	PC2	PC3	PC4	PC5
t	-0.73	0.06	0.05	-0.23	0.65
[Z/H]	0.58	-0.48	-0.01	-0.24	0.61
[E/Fe]	-0.19	-0.52	0.38	0.73	0.06
FUV-NUV	0.14	0.26	0.92	-0.26	-0.02
$\sigma$	-0.29	-0.65	0.07	-0.53	-0.45
Eigenvalue	1.64	1.42	0.97	0.76	0.21
Percentage of variance	32.89	28.43	19.38	15.14	4.18
Cumulative percentage	32.89	61.30	80.68	95.82	100.00

Table 2: Principal component analysis: the total sample.

**The UV-weak sample** There are 188 galaxies in this sample which are classified as UV-weak.

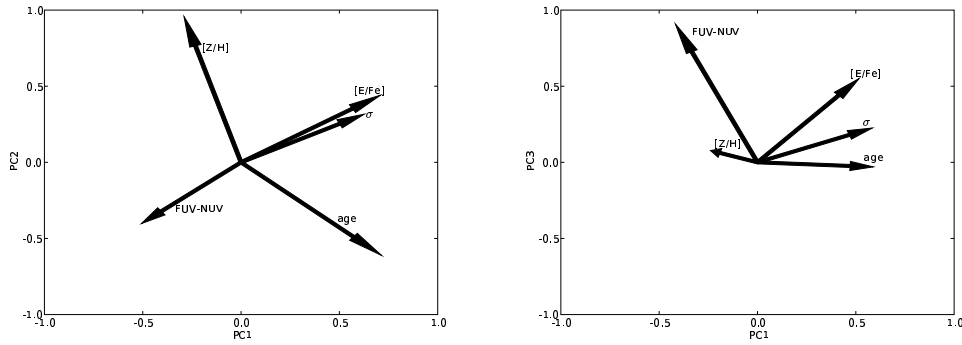


Figure 15: Principal components: The UV-weak sample.

Variable	PC1	PC2	PC3	PC4	PC5
t	0.54	-0.46	-0.03	-0.29	0.64
[Z/H]	-0.22	0.72	-0.07	-0.24	0.60
[E/Fe]	0.47	0.24	0.51	0.67	0.09
FUV-NUV	-0.38	-0.30	0.83	-0.25	0.03
$\sigma$	0.54	0.33	0.21	-0.59	-0.46
Eigenvalue	1.86	1.53	0.78	0.65	0.19
Percentage of variance	37.14	30.55	15.63	12.96	3.72
Cumulative percentage	37.14	67.69	83.32	96.28	100.00

Table 3: Principal component analysis: the UV-weak sample

**The UV-strong sample** There are 121 galaxies which are classified as UV-strong.

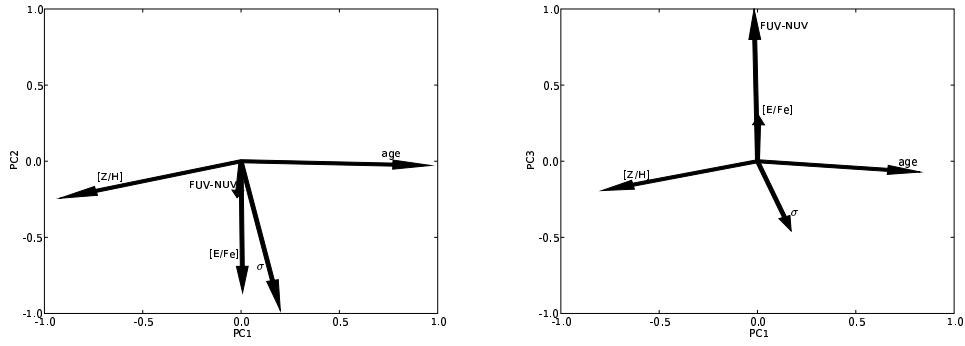


Figure 16: Principal components: The UV-strong sample.

Variable	PC1	PC2	PC3	PC4	PC5
t	0.71	-0.02	-0.06	-0.10	-0.69
[Z/H]	-0.68	-0.18	-0.17	-0.19	-0.66
[E/Fe]	0.01	-0.64	0.26	0.72	-0.11
FUV-NUV	-0.02	-0.18	0.86	-0.47	0.02
$\sigma$	0.15	-0.73	-0.40	-0.46	0.28
Eigenvalue	1.74	1.11	1.02	0.92	0.21
Percentage of variance	34.76	22.27	20.36	18.49	4.12
Cumulative percentage	34.76	57.04	77.39	95.88	100.00

Table 4: Principal component analysis: the UV-strong sample

## 5 Discussion

In this study, it was hypothesized that an anti-correlation between FUV-NUV colour and single stellar population age is present in early-type galaxies, analogous to the relation of  $H\beta$  to age, as seen in Figure 17. From the figure it is evident that there exist some degeneracies in the relation between the age and  $H\beta$  line strength. This degeneracy is overcome by applying the Worthey models to the Lick/IDS indices as described by Trager et al. (2000a and 2000b) and Trager et al. (2005).

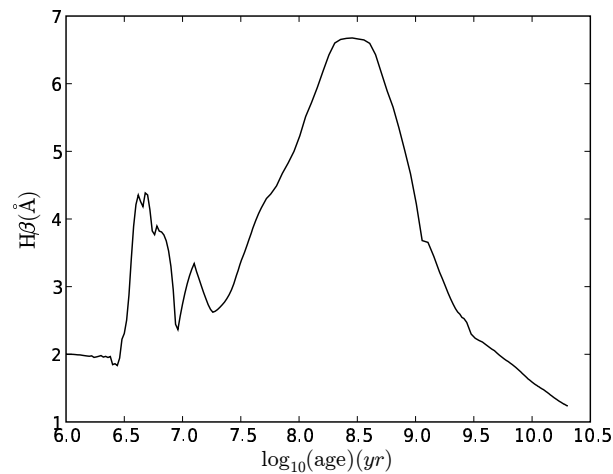


Figure 17: Evolution of the  $H\beta$  line strength with age of a stellar population of solar metallicity, calculated using the Bruzual and Charlot (2003) stellar models.

The behaviour of the far-UV flux as a function of age has been investigated by Yi et al. (1999), and is shown in figure 3. Here, as well as with the  $H\beta$  line strength as an age indicator, a degeneracy in the relation between far-UV flux and stellar population age is obvious. Bruzual and Charlot also show an age-dependence for the FUV-NUV colour, although without the asymptotic behaviour at young ages.

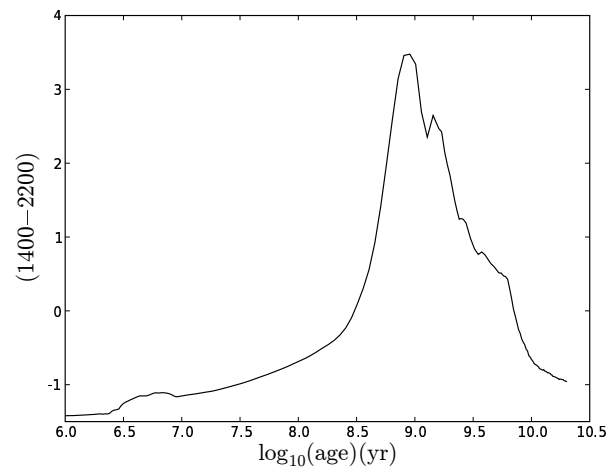


Figure 18: UV-colours from the Bruzual and Charlot (2003) stellar population models.

In figure 9, we show UV data taken from the literature (Dorman et al. 1995) combined with SSP ages. From this plot a trend can be inferred by which the (15-25) colour (as an equivalent to the FUV-NUV colour taken from *GALEX*) decreases with the SSP age of a population. This would indicate the presence of an initially UV-strong population decreasing in strength with age.

The distribution in age and metallicity is shown in figure 11. While the average error in the  $H\beta$  is comparable to that found by Trager et al. (2000a), the spread in the  $\langle Fe \rangle$  is much larger than found by Trager et al. An estimate of  $[E/Fe]$  using the right panel of figure 11 can therefore not be considered to be very reliable.

In our attempt to classify the galaxies by UV-flux in the same way as Yi et al. (2005), we found that the discrepancy between the magnitudes adjusted to the isophotal profile of the galaxy and those from the fixed apertures caused some mixing between the classifications, as can be seen in figure 11.

The principal component analysis which was performed on the sample and two subsets as defined by the UV-strong and the UV-weak classification respectively shows some interesting correlations. In the total sample, we see the  $t - [Z/H] - [E/Fe] - \sigma$  hyperplane as described in Trager et al. (2000b). In the PC1-PC2 plane, the FUV-NUV colour shows a strong anti-correlation with both  $[E/Fe]$  and the velocity dispersion,  $\sigma$ , i.e. galaxies with bluer FUV-NUV colours would generally have either a strong  $[E/Fe]$  or a high velocity dispersion, or both. However, the first two principal components contain only 61.3 % of the variance in the sample, while it is recommended to use a set of axis containing at least 75 % of the variance to reduce the dimensionality of the problem. This means we have to include the third principal component into our analysis. Taking the right panel of figure 14 into account, we find that the FUV-NUV colour is still largely uncorrelated with either age or metallicity, but the strong anti-correlation with  $[E/Fe]$  and  $\sigma$  seems to be less significant, with a lack of correlation with  $\sigma$  and a weak correlation with  $[E/Fe]$ . The UV-weak sample shows a trend which is more or less similar to that of the total sample, albeit with some differing correlations in the PC1-PC3 plane. The UV strong sample, however, shows only a weak correlation between the  $[E/Fe]$  and the FUV-NUV.

We hypothesise that we see the combined effects of several populations in this analysis. In the UV-weak case, we see a UV-active population which is uncorrelated to the population which is prominent in the optical spectra. There might be some correlation with the enhancement factor,  $[E/Fe]$ , but this is uncertain. The UV-strong class probably shows the same two populations, with another, which is highly correlated with  $[E/Fe]$ , 'filling in' the contribution of the UV-population which we see in the UV-weak class.

The above would seem to suggest a dependence of the strength of the UV-flux on the chemical content. Various authors have found that the metallicity has a large impact on the UV-flux (Yi et al. 1999, Brown et al. 2000) since the envelope mass of the EHB stars is highly dependent on the metallicity. The anti-correlation of the FUV-NUV with  $\sigma$  might be an indication of an increase of the FUV-NUV colour with stellar mass for the UV-weak galaxies.

---

## 6 Conclusion

We have analysed the ultraviolet colours of early-type galaxies drawn from the *SDSS* and *GALEX* databases, with the intention of finding a correlation between the SSP age derived from optical spectroscopy and the FUV-NUV colour from the *GALEX* observations. The data from the *SDSS* spectra were analysed using the method developed by Trager et al. (2000,2005), with emission line data drawn from the MPA-Garching database. The *GALEX* data was corrected for reddening using the UV extinction relation developed by Cardelli, Clayton and Mathis (1989) and colour excesses derived from the Schlegel (1998) dustmaps which were given by the *GALEX* pipeline.

The galaxies were classified in three UV-classes as was also done by Yi et al. (2005), and a principal component analysis was performed on two of these classes (due to the low number of galaxies in the UV-intermediate class the analysis was considered to be irrelevant) and on the entire sample.

We found that the UV-flux of the galaxies in our sample is uncorrelated with the SSP age. The UV-flux shows a very weak correlation with the velocity dispersion and the enhancement factor in the UV-strong class of galaxies, while it is strongly anti-correlated with these parameters in the weak classification, and in the total sample.

## References

- Bernardi, M., Sheth, R.K., Annis, J., et al. 2003, *AJ*, 1817
- Bertola, F., Cappacioli, M., Holm, A.V., Oke, J.B., 1980, *ApJ*, 237, L65
- Bertola, F., Cappaciolo, M., Oke, J.B., 1982, *ApJ*, 254, 494
- Bianchi, L., Seibert, M., Zheng, W., Thilker, D.A., Friedman, P.G., Wyder, T.K., Donas, J., et al., 2005, *ApJ*, 619, L27
- Binney, J, Merrifield, M, 1998, *Galactic astronomy*, Princeton University Press
- Blanton, M.R., Roweis, S., 2003, *AJ*, 125, 2348
- Burstein, D., Bertola, F., Buson, L.M., Faber, S.M., Lauer, T.R., 1988, *ApJ*, 328, 440
- Brown, T.M., Bowers, C.W., Kimble, R.A., Sweigart, A.V., 2000, *ApJ*, 532, 308
- Cardelli, J.A., Clayton, G.C., Mathis, J.S., 1989, *ApJ*, 345, 245
- Code, A.D., *PASP*, 1969, 81, 475
- Code, A.D., Welch, G.A., 1979, *ApJ*, 228, 95
- Connolly, A.J., Szalay, A.S., Bershad, M.A., Kinsey, A.L., Calzeth, D., 1995, *AJ*, 110, 1071
- Connolly, A.J., Szalay, A.S., 1999, *AJ*, 117, 2052
- Dorman, B., O'Connell, R.W., Rood, R.T., 1995, *ApJ*, 442, 105
- Faber, S.M., 1983, *Highlights Astr.*, 6, 165
- Fisher, D., Franx, M., Illingworth, G., 1996, *ApJ*, 459, 110
- Fukugita, M., Ichikawa, T., Gunn, J.E., Doi, M., Shimasaku, K., Schneider, D.P., 1996, *AJ*, 111(4), 1748
- González, J.J., 1993, Ph.D. thesis, Univ. California, Santa Cruz
- Greggio, L., Renzini, A., 1990, *ApJ*, 364, 35
- Gunn, J.E., Stryker, L.L., Tinsley, B.M., 1981, *ApJ*, 249, 48
- Hills, J.G., 1971, *ApJ*, 12, 1
- Kewley, Dopita, Evans, Groves, Sutherland, Binette, Allen, Leitherer, 2004, *in preparation*
- Kuntschner, H., 2000, *MNRAS*, 315, 184
- Kippenhahn, R., Weigert, A., 1994, *Stellar structure and evolution*, 3<sup>rd</sup> ed., Springer-Verlag
- Kondo, Y., ed., 1987, *Exploring the universe with the IUE satellite*, Dordrecht: Reidel
- Martin, D.C. et al. 2005, *ApJ*, 619, L1
- Moore, S.A.W., Lucey, J.R., Kuntschner, H., Colless, M., 2002, *MNRAS*, 336, 382
- Murtagh, F., Heck, A., 1987, *Multivariate Data analysis*, Kluwer
- O'Connell, R.W., *ARA&A*, 1999, 37, 603
- Oke, J.B., Bertola, F., Cappacioli, M., 1981, *ApJ*, 243, 453

- 
- Peterson, R.C., Carney, B.W., Dorman, B., Green, E.M., Landsman, W., Liebert, J., O'Connell, R.W., Rood, R.T., ApJ, 2003, 588,299
  - Ryden, B.S., 2003, *Introduction to Cosmology*, Addison Wesley
  - Sadler, E.M., Oosterloo, T.M., Morganti, R., Karakas, A., 2000, ApJ, 119,1180
  - Schlegel, D.J., Finkbeiner, D.P., Davis, M., 1998, ApJ, 500, 525
  - Stoughton, C., Lupton, R.H., et al., 2002, AJ, 123, 485
  - Tinsley, B.M., 1972, ApJ, 178, 319
  - Trager, S.C., Worthey, G., Faber, S.M., Burstein, D., González, ApJSS, 1998, 116, 1
  - Trager, S.C., Faber, S.M., Worthey, G., González, J.J., 2000, ApJ, 119, 1645 (Trager et al. 2000a)
  - Trager, S.C., Faber, S.M., Worthey, G., González, J.J., 2000, ApJ, 120, 165 (Trager et al. 2000b)
  - Trager, S.C., Worthey, G., Faber, S.M., Dressler, A., 2005, MNRAS, 362, 2
  - Tremonti, C.A., Heckman, T.M., Kauffman, G., 2004, ApJ, 613, 898
  - Welch, G.A., 1982, ApJ, 259, 77
  - Yi, S.K., Lee, Y., Woo, J., Park, J., Demarque, P., Oemler, A., 1999, ApJ, 513, 128
  - Yi, S.K. et al, ApJ, 2005, 619, L111

## A Data access in *SDSS* and *GALEX*

Both the Sloan Digital Sky Survey as the *GALEX* mission have generated vast amounts of data. This data has been made publicly available on the web, at <http://cas.sdss.org/astrodr3/en/> (for *SDSS*, under SQL search) and <http://galex.stsci.edu/GR1/?page=sqlform> (for *GALEX*, under Data search). I will discuss the structure of a standard SQL<sup>10</sup> query first, and in following paragraphs I will discuss the specific tables and other services used for data access in the course of this project.

**Queries** A SQL query consists of three parts:

1. **SELECT** This field specifies the parameters to be extracted.
2. **FROM** This field contains the tables you want to extract the data from.
3. **WHERE** This field specifies the exact conditions you want to impose on the search.

For example:

```
SELECT g.objid,g.sdssobjid, p.ra, p.dec, p.band, p.glon, p.glat, p.nuv_mag,
p.nuv_magerr, p.fuv_mag, p.fuv_magerr, p.e_bv
FROM
photoobjall as p,
galexsdssdr3 as g
WHERE p.objid = g.objid
and g.dist <= 6
and p.objtype = 0
and p.band=3 /* band = NUV and FUV*/
```

The example above shows a query which extracts object identifiers for both *GALEX* and *SDSS*, right ascension and declination, galactic coordinates and FUV and NUV fluxes from the *GALEX* database. The tables it extracts the information from are photoobjall, which contains all photometric information for the objects in the survey, and galexsdssdr3, which contains the *SDSS* object identifiers corresponding to the *GALEX* objects. The tables are aliased to p and g to keep the query somewhat readable using the “as” statement. The first statement in the WHERE part is a so-called “inner join”, which means that only objects which are present in both tables are returned. The other parameters specify the maximum distance between objects in *GALEX* and *SDSS*, the specific object type (0 denotes a galaxy, 1 a star and -1 means the type is unknown), and the number of bands which are observed.

***GALEX*** A typical SQL query for *GALEX* was already listed in the previous paragraph, and it already showed two of the most important tables in the dataset. Photoobjall contains fluxes and magnitudes and other photometric properties for various apertures. Galexsdssdr3 contains, as already mentioned the *SDSS* object identifiers for those *GALEX* objects that are present in the *SDSS* Third Data Release.

***SDSS*** For the purpose of this project, we needed the 1d spectra for the galaxies which were present in our queries. These can be downloaded using the *SDSS* Data archive server, or DAS. The spectra are identified by three numbers: the modified julian day, the fiberID and the plateID. The *SDSS* database has, just like the *GALEX* database, a “Schema browser”, a listing of all the contents of the database. The *SDSS* data is listed in *tables*. These list all the parameters for each

---

<sup>10</sup>SQL: Structured Query Language

image or spectrum, but often they contain an overload of data. To speed up searches, subsets of the tables are listed in *views*. For example, the parameters we required to find the relevant *SDSS* spectra were listed in the view *specobj*. These parameters are listed in the view *specobj*, which also contains the parameter *bestobjID*, the best estimate for the photometric object which the spectrum corresponds to. Other tables we used are *photobj* and *specphotoall*, since they contain variables we needed to incorporate the Bernardi et al.(2003) criteria.

**CasJobs** As a final note on the data access for both *SDSS* and *GALEX*, we would like to discuss the CasJobs service for the databases. It is possible to create a free account under CasJobs, which allows you to upload lists of objects and store the results from queries online. This service is mandatory for *SDSS* when uploaded files exceed 80 KB, queries take more than 3600 seconds to run or the output dataset exceeds 500.000 objects.

## B Principal Component Analysis

The following pages are a summary of chapter 2 of *Multivariate Data Analysis* by Murtagh and Heck, which also lists a FORTRAN 77 code to perform principal component analysis, but since this book is notoriously hard to obtain from the RuG library system the author found a short description of the technique in order.

**Introduction** When dealing with multidimensional data (in our case a set of galaxies with SSP properties, line strengths and UV colours and -fluxes) principal component analysis (PCA) can be used to analyse the correlations between these parameters. PCA determines axes within a dataset along which the variance is greatest, and thus reduces the dimensionality of the problem. E.g. Trager et al. (2000b) use PCA to determine that elliptical galaxies populate a plane in the age-[Z/H]-[E/Fe] -  $\sigma$  space.

**Mathematical description** A dataset of  $n$  objects with  $m$  variables can be described by a matrix  $X = \{x_{ij}\}$ , where  $i$  denotes a member of the collection of objects in  $\mathbb{R}^n$  and  $j$  a member of the collection of variables,  $\mathbb{R}^m$ . PCA searches for the best-fitting set of orthogonal axes to replace the initially given  $m$  axes in this space. At the same time, a similar procedure is carried out on  $\mathbb{R}^n$ . The axis which fits the points in  $\mathbb{R}^m$  is determined first.

The goodness of fit of this axis to the points is defined as the squared deviation of the points from the axis. Minimizing the sum of the distances of the points from the new axis is equivalent to maximising the sum of the squared projections on the axis, in effect maximising the variance of the points when projected on the axis.

The squared projection of points on the new axis, for all points, is

$$(X\mathbf{u})'(X\mathbf{u}).$$

Since this form would increase indefinitely if  $\mathbf{u}$  were arbitrarily large,  $\mathbf{u}$  is chosen to be of unit length, i.e.  $\mathbf{u}'\mathbf{u} = 1$ . We want to maximise the quadratic form  $\mathbf{u}'S\mathbf{u}$ , ( $S = X'X$ ) with the constraint that  $\mathbf{u}'\mathbf{u} = 1$ . This is done by setting the derivative of the Lagrangian equal to zero. The Lagrangian is given by:

$$\mathbf{u}'S\mathbf{u} - \lambda(\mathbf{u}'\mathbf{u})$$

Where  $\lambda$  is a Lagrange multiplier. Differentiation gives:

$$2S\mathbf{u} - 2\lambda\mathbf{u}.$$

The optimal value of  $\mathbf{u}$  is the solution of:

$$S\mathbf{u} = \lambda\mathbf{u}$$

$\mathbf{u}$  is thus the eigenvector associated with the eigenvalue  $\lambda$  of matrix  $S$ . It is thus the axis sought, and the eigenvalue is an indication of the amount of variance explained by the axis. The second axis is orthogonal to the first, i.e.  $\mathbf{u}'\mathbf{u}_1 = 0$ , and it satisfies the equation:

$$\mathbf{u}'X'X\mathbf{u} - \lambda_2(\mathbf{u}'\mathbf{u} - 1) - \mu_2(\mathbf{u}'\mathbf{u}_1)$$

Differentiating this gives:

$$2S\mathbf{u} - 2\lambda_2\mathbf{u} - \mu_2\mathbf{u}_1$$

Setting this equal to zero and multiplying across by  $\mathbf{u}'_1$  implies that  $\mu_2$  must be equal to zero. Therefore,  $\mathbf{u}_2$  is another solution of  $S\mathbf{u} = \lambda\mathbf{u}$ .  $\lambda_2$  and  $\mathbf{u}_2$  are thus the second eigenvalue and associated eigenvector of  $S$ .

The eigenvectors of  $S = X'X$ , arranged in descending order of corresponding eigenvalues, give the line of best fit to the cloud of points, the plane of best fit, the three-dimensional hyperplane of

best fit, and so on for higher-dimensional subspaces.  $X'X$  is called the *sums of squares and cross products* matrix.

It is possible to find zero-value eigenvalues. This indicates that the dimensionality of the space is actually less than expected (e.g. the points might lie on a plane in a three-dimensional space).

In  $\mathbb{R}^n$ , a PCA analogous to that described above may be carried out, with the line of best fit,  $\mathbf{v}$ , the following is to be maximised:

$$(X'\mathbf{v})'(X'\mathbf{v}), \text{ where } \mathbf{v}'\mathbf{v} = 1,$$

And:

$$XX'\mathbf{v}_1 = \mu_1\mathbf{v}_1$$

Combining this with the  $\mathbb{R}^m$  case:

$$(X'X)(X\mathbf{u}_1) = \lambda_1(X\mathbf{u}_1),$$

which yields  $\lambda_1 = \mu_1$ .

The relation between the  $k^{\text{th}}$  eigenvectors (these being of unit length) in  $\mathbb{R}^m$  and  $\mathbb{R}^n$  is given by:

$$\mathbf{v}_k = \frac{1}{\sqrt{\lambda_k}}X\mathbf{u}_k$$

and

$$\mathbf{u}_k = \frac{1}{\sqrt{\lambda_k}}X'\mathbf{v}_k$$

This means that the eigenvalues  $\lambda$  are the same in both spaces, and there is a simple linear transformation which maps the optimal axes in one space into those of the other. The variance of the projections onto a given axis in  $\mathbb{R}^m$  is given by  $(X\mathbf{u})'(X\mathbf{u})$ , which is equal to  $\lambda$ .

Since PCA in  $\mathbb{R}^m$  and  $\mathbb{R}^n$  leads to finding  $n$  and  $m$  eigenvalues, and since it has been seen that these eigenvalues are equal, it follows that the number of *non-zero* eigenvalues has to be equal to or less than  $\min(m, n)$ .

The eigenvectors associated with the  $p$  largest eigenvalues yield the best-fitting  $p$ -dimensional subspace of  $\mathbb{R}^m$ . A measure of the approximation is the percentage of the approximation explained by the subspace

$$\frac{\sum_{k \leq p} \lambda_k}{\sum_{k=1}^n \lambda_k}$$

An alternative view of the PCA is given by the Karhunen-Loève expansion. This is derived by multiplying the summed relation between the unitary vectors in  $\mathbb{R}^m$  and  $\mathbb{R}^n$  by  $\mathbf{u}'_k$ , which gives:

$$X \sum_{k=1}^n \mathbf{u}_k \mathbf{u}'_k = \sum_{k=1}^n \sqrt{\lambda_k} \mathbf{v}_k \mathbf{u}'_k$$

Since  $\sum_{k=1}^n \mathbf{u}_k \mathbf{u}'_k = \mathbf{1}$ , we get:

$$X = \sum_{k=1}^n \sqrt{\lambda_k} \mathbf{v}_k \mathbf{u}'_k$$

Thus, the first  $p$  eigenvectors can therefore approximate the original matrix by:

$$\mathcal{X} = \sum_{k=1}^p \sqrt{\lambda_k} \mathbf{v}_k \mathbf{u}'_k$$

For a  $p$  which is considerably smaller than  $n$ , and  $\mathcal{X}$  approximately equal to  $X$ , we thus have a far more economical description.

Apart from the PCA on the sums of squares and cross products matrix discussed above, it is also possible to perform PCA on a correlation matrix, which consists of values which have been standardised by the following procedure:

$$x_{ij} = \frac{r_{ij} - \bar{r}_j}{s_j \sqrt{n}}$$

where

$$\bar{r}_j = \frac{1}{n} \sum_{i=1}^n r_{ij} \text{ and } s_j^2 = \frac{1}{n} \sum_{i=1}^n (r_{ij} - \bar{r}_j)^2$$

The matrix to be diagonalized is then the correlation matrix, given by:

$$\rho_{jk} = \frac{1}{n} \sum_{i=1}^n (x_{ij} - x_{ik})^2 = \frac{1}{n} \sum_{i=1}^n (r_{ij} - \bar{r}_j)(r_{ik} - \bar{r}_k) / s_j s_k$$

Analysis on a matrix with terms  $\rho_{jk}$  is PCA on a *correlation* matrix.

If centring of the data is acceptable, but the rescaling of the variance is not, the matrix of  $(i,j)^{th}$  term

$$c_{jk} = \frac{1}{n} \sum_{i=1}^n (r_{ij} - \bar{r}_j)(r_{ik} - \bar{r}_k)$$

**Visualisation** To properly visualise the relation between the principal components and the variables, we have used vector plots in which the vectors show the projections of the eigenvectors corresponding to the variables onto the principal components. We choose to show only the principal components which contain  $\geq 75\%$  of the variance. In this visualisation, projections which are close to each other (i.e. parallel vectors) indicate a correlation between the two variables, while an anti-correlation is indicated by two vectors oriented in opposite directions. Two vectors oriented orthogonally to each other indicate a lack of correlation.

## C Code

**Reddening correction** The following functions in Python determine the extinction in the UV and optical bands used.

```
def reddening_corr_fiber(lambd,e_bv):
    R_v = 3.3
    lambd = float(lambd)*(10**-4)
    x = 1/lambd
    if (1.1 <= x <= 3.3): #Optical
        y = (x-1.82)
        a = 1+0.17699*y - 0.50447*y**2 -0.02427*y**3+0.72085*y**4 + 0.01979*y**5
        - 0.77530*y**6 + 0.32999*y**7
        b = 1.41338*y + 2.28305*y**2 + 1.07233*y**3 - 5.38434*y**4 - 0.62251*y**5
        - 2.09002*y**7
    A_lambd = (a*R_v*e_bv) + (b * e_bv)
    return A_lambd

def reddening_corr_UV(lambd,e_bv):
    """
    Produces reddening corrections for UV-magnitudes using the method listed by
    Cardelli, Clayton and Mathis(1989)

    """
    R_v = 3.3 #Rough average from plot in Binney and Merrifield
    lambd = float(lambd)*(10**-4)
    x = 1/lambd
    a = 0
    b = 0
    if (x < 5.9):
        F_a = 0
        F_b = 0
    if (8 >= x >= 5.9):
        F_a = -0.04473*(x-5.9)**2 - 0.009779*(x-5.9)**3
        F_b = 0.2130*(x-5.9)**2 + 0.1207*(x-5.9)**3
        a = 1.752-0.316*x-(0.104/((x-4.67)**2+0.341))+F_a
        b = -3.090 + 1.825*x+(1.206/((x-4.62)**2 + 0.263))+F_b
    #Calculate the absorption:
    A_lambd = (a * R_v * e_bv) + (b * e_bv)
    return A_lambd
```